The mitochondrial protein PGAM5 suppresses energy consumption in brown adipocytes by repressing expression of uncoupling protein 1

Received for publication, October 17, 2019, and in revised form, March 4, 2020 Published, Papers in Press, March 6, 2020, DOI 10.1074/jbc.RA119.011508

Sho Sugawara[‡], Yusuke Kanamaru[‡], Shiori Sekine[‡1], Lila Maekawa[‡], Akinori Takahashi[§], Tadashi Yamamoto[§¶], Kengo Watanabe[‡], Takao Fujisawa[‡], Kazuki Hattori[‡2], and Hidenori Ichijo[‡3]

From the [‡]Laboratory of Cell Signaling, Graduate School of Pharmaceutical Sciences, University of Tokyo, 7-3-1 Hongo, Bunkyo-ku, Tokyo 113-0033, Japan, the [§]Cell Signal Unit, Okinawa Institute of Science and Technology Graduate University, 1919-1 Tancha, Onna, Okinawa 904-0495, Japan, and the [¶]Laboratory for Immunogenetics, Center for Integrative Medical Sciences, RIKEN, 1-7-22 Suehiro-cho, Tsurumi-ku, Yokohama City, Kanagawa 230-0045, Japan

Edited by Qi-Qun Tang

Accumulating evidence suggests that brown adipose tissue (BAT) is a potential therapeutic target for managing obesity and related diseases. PGAM family member 5, mitochondrial serine/threonine protein phosphatase (PGAM5), is a protein phosphatase that resides in the mitochondria and regulates many biological processes, including cell death, mitophagy, and immune responses. Because BAT is a mitochondria-rich tissue, we have hypothesized that PGAM5 has a physiological function in BAT. We previously reported that PGAM5-knockout (KO) mice are resistant to severe metabolic stress. Importantly, lipid accumulation is suppressed in PGAM5-KO BAT, even under unstressed conditions, raising the possibility that PGAM5 deficiency stimulates lipid consumption. However, the mechanism underlying this observation is undetermined. Here, using an array of biochemical approaches, including quantitative RT-PCR, immunoblotting, and oxygen consumption assays, we show that PGAM5 negatively regulates energy expenditure in brown adipocytes. We found that PGAM5-KO brown adipocytes have an enhanced oxygen consumption rate and increased expression of uncoupling protein 1 (UCP1), a protein that increases energy consumption in the mitochondria. Mechanistically, we found that PGAM5 phosphatase activity and intramembrane cleavage are required for suppression of UCP1 activity. Furthermore, utilizing a genome-wide siRNA screen in HeLa cells to search for regulators of PGAM5 cleavage, we identified a set of candidate genes, including phosphatidylserine decarboxylase (*PISD*), which catalyzes the formation of phosphatidylethanolamine at the mitochondrial membrane. Taken together, these results indicate that PGAM5 suppresses mitochondrial energy expenditure by down-regulating UCP1 expression in brown adipocytes and that its phosphatase activity and intramembrane cleavage are required for UCP1 suppression.

Obesity, which is characterized by excess adiposity, is a significant risk factor for various chronic diseases, such as cardiovascular diseases and type 2 diabetes (1). Several anti-obesity drugs have been approved worldwide; however, safety and efficacy concerns cause patients and doctors to hesitate to use them (2). Adipose tissue is the central organ involved in storing resting energy in the form of triacylglycerol, and there are two major types of adipose tissues in mammals: white adipose tissue (WAT)[4] and brown adipose tissue (BAT). WAT is the greatest storage unit; white adipocytes harbor large unilocular lipid droplets and release fatty acids as an energy source when energy demand becomes higher than energy intake. Meanwhile, BAT actively gives off energy in the form of heat in response to cold stress or energy excess, and this process is referred to as adaptive thermogenesis (3). BAT has small, multilocular lipid droplets; however, it is rich in mitochondria that specifically express UCP1, which is predominantly responsible for the thermogenic function (4). Activated UCP1 consumes the proton gradient produced by the mitochondrial electron transport chain, and this proton pump-and-leak cycle reduces mitochondrial membrane potential, which results in high levels of substrate oxidation and heat generation (3–5). The molecular basis of the transcriptional induction mechanisms for *Ucp1* has been widely

This work was supported by a Grant-in-Aid for Scientific Research (KAKENHI) from the Japan Society for the Promotion of Science (JSPS; Grants JP25221302, JP18H03995, JP16K15115, JP16K18872, and JP17K15086), the Project for Elucidating and Controlling Mechanisms of Aging and Longevity from the Japan Agency for Medical Research and Development (AMED; Grant JP19gm5010001), and Kowa Life Science Foundation Grant 2016 A-2. The authors declare that they have no conflicts of interest with the contents of this article.

This article contains Tables S1–S3 and Figs. S1–S3.

[1] Present address: Aging Institute, Division of Cardiology, Dept. of Medicine, University of Pittsburgh, 100 Technology Dr., Pittsburgh, PA 15219.

[2] To whom correspondence may be addressed: Center for Nanomedicine and Division of Engineering in Medicine, Dept. of Medicine, Brigham and Women's Hospital, Harvard Medical School, 60 Fenwood Rd., Boston, MA 02115. E-mail: kzkhattori@13.alumni.u-tokyo.ac.jp.

[3] To whom correspondence may be addressed: Laboratory of Cell Signaling, Graduate School of Pharmaceutical Sciences, University of Tokyo, 7-3-1 Hongo, Bunkyo-ku, Tokyo 113-0033, Japan. Tel.: 81-3-5841-4858; Fax: 81-3-5841-4798; E-mail: ichijo@mol.f.u-tokyo.ac.jp.

[4] The abbreviations used are: WAT, white adipose tissue; BAT, brown adipose tissue; PGAM5, phosphoglycerate family member 5; PARL, presenilin-associated rhomboid-like; PISD, phosphatidylserine decarboxylase; IMM, inner mitochondrial membrane; TM, transmembrane; iBAT, interscapular brown adipose tissue; iWAT, inguinal white adipose tissue; KO, knockout; CCCP, carbonyl cyanide *m*-chlorophenyl hydrazone; FCCP, carbonyl cyanide *p*-trifluoromethoxyphenylhydrazone; OCR, oxygen consumption rate; IB, immunoblotting; ICC, immunocytochemistry; ROI, region of interest; PS, phosphatidylserine; PE, phosphatidylethanolamine; qRT-PCR, quantitative RT-PCR; Etn, ethanolamine; CHO, Chinese hamster ovary; Ch., Channel; TRITC, tetramethylrhodamine isothiocyanate.

studied. For instance, the mitogen-activated protein kinase cascade and the cAMP-dependent protein kinase– cAMP-responsive element-binding protein axis induce *Ucp1* expression (6). However, mechanisms driving the negative regulation of *Ucp1* are poorly understood, except for some reports regarding RIP140 (receptor-interacting protein 140) and liver X receptor (7–9). Although boosting energy expenditure by activating UCP1 is a promising strategy for obesity, maintaining an appropriate amount of UCP1 is also important because highly active UCP1 can exacerbate atherosclerosis in mice (10), and, conversely, *Ucp1* deficiency leads to obesity in mice (11). BAT was once thought to be active only in rodents and human infants, but a growing body of evidence indicates that adult humans can also have an active form of BAT (12–15). Hence, BAT is a potential therapeutic target for the treatment of obesity and its related serious complications.

Phosphoglycerate mutase family member 5 (PGAM5) is a protein phosphatase that is localized to mitochondria via its N terminus (16, 17); through its phosphatase activity, PGAM5 is involved in many biological processes, such as cell death, mitophagy, and immune responses (18–22). We previously revealed that PGAM5 is mainly localized at the inner mitochondrial membrane (IMM) because of its N-terminal transmembrane (TM) domain, and it is cleaved within the TM domain by presenilin-associated rhomboid-like (PARL), an IMM-resident protease, in response to mitochondrial membrane potential loss (23). Additionally, another group and our group reported that OMA1, a zinc metalloprotease, is also responsible for the cleavage of PGAM5 (23, 24). A recent study showed that cytosolic PGAM5 dephosphorylates and stabilizes β-catenin, resulting in mitochondrial biogenesis (25). Further, another study revealed that the cleaved form of PGAM5 sensitizes cells to apoptosis induced by staurosporine (19). Although these results suggest the physiological reasons behind PGAM5 cleavage, the precise mechanisms of cleavage remain unclear.

With respect to the physiological functions of PGAM5, PGAM5-knockout (KO) mice show Parkinson's-like movement disorder, suggesting the role of PGAM5 in brain (26). Another report demonstrated that PGAM5-KO mice show resistance to concanavalin A-induced liver injury (27). However, there have been no reports on the energy metabolism-related functions of PGAM5. Because BAT is a mitochondria-rich organ, we assessed the physiological functions of PGAM5 by analyzing PGAM5-KO mice and revealed that these mice are resistant to severe metabolic stress (28). Importantly, the accumulation of lipids in BAT was dramatically suppressed even in nonstimulated conditions, raising the possibility that lipid consumption is increased in the absence of PGAM5 (28). However, the underlying mechanisms by which PGAM5 regulates lipid homeostasis in BAT are not fully known.

Here, we show that mitochondria-resident phosphatase PGAM5 acts as a negative regulator of energy expenditure in brown adipocytes, and this regulation is achieved at least in part by suppressing *Ucp1* expression. Both phosphatase activity and intramembrane cleavage are required for the suppressive effects of PGAM5 on *Ucp1* expression. Additionally, we utilized an image-based genome-wide siRNA screen system to identify PGAM5 cleavage regulators, and we identified a set of candidate genes, including phosphatidylserine decarboxylase (*PISD*).

Results

PGAM5 depletion augments UCP1 expression in brown adipocytes

In our previous study, we reported that PGAM5-KO mice showed resistance to high fat diet–dependent obesity and decreased lipid accumulation in interscapular BAT (iBAT) (28). To understand the underlying mechanisms behind these outcomes, we first performed RNA-Seq analysis using iBAT from WT and PGAM5-KO mice. Genes important for iBAT functions are shown in the heat map, which shows that most of the genes were not significantly different between WT and PGAM5-KO iBAT (Fig. S1*A*). Among these data, we found that mRNA levels of *Ucp1*, a gene that is critical for the thermogenic functions of brown adipocytes, were significantly increased in PGAM5-KO iBAT (Fig. 1*A*). Other down-regulated genes (*blue dots* in Fig. 1*A*) and up-regulated genes (*red dots* in Fig. 1*A*) in PGAM5-depleted tissue are listed in Table S1*A*. To confirm the results of RNA-Seq, we next performed quantitative RT-PCR (qRT-PCR) analysis and verified that *Ucp1* mRNA was significantly increased in iBAT from PGAM5-KO mice (Fig. 1*B*). However, the mRNA expression levels of several other genes that are critical for brown adipocyte functions, such as *Cidea*, *Dio2*, *Elovl3*, *Ppargc1a*, and *Prdm16*, were almost equivalent in WT and PGAM5-KO iBAT (Fig. 1*B*). Similarly, the protein abundance of UCP1 was increased in PGAM5-KO iBAT, but there were minimal changes in another mitochondria-resident protein, UQCRC1 (Fig. 1*C*). These data suggest that PGAM5 selectively suppresses *Ucp1* expression in iBAT. Given the results from the iBAT of PGAM5-KO mice (Fig. 1, *B* and *C*), we examined the gene expression levels of inguinal WAT (iWAT) as well because *Ucp1* expression can be induced in iWAT under several conditions, such as chronic cold acclimation, exercise, long-term treatment with the β_3-adrenergic receptor agonist, and cancer cachexia (29). We found that both mRNA and protein expression of UCP1 exhibited an increasing trend in iWAT from PGAM5-KO mice (Fig. S1, *B* and *C*).

We next tested whether the increase of UCP1 expression in PGAM5-KO iBAT is cell-autonomous by analyzing primary cultures of brown adipocytes. Triglyceride accumulation was evaluated by Oil Red O staining, and we found that there was no obvious difference between WT and PGAM5-KO adipocytes on day 6 (Fig. 1*D*). To evaluate protein expression levels, cell lysates were prepared on alternating days throughout adipocyte differentiation. We found that the protein abundance of UCP1 was increased in differentiated PGAM5-KO adipocytes on days 6 and 8 (Fig. 1*E*), which agreed with the *in vivo* results (Fig. 1*C*). We also confirmed that the mRNA expression levels of *Ucp1* were increased in PGAM5-KO adipocytes on day 6 (Fig. 1*F*). Consistent with the data from iBAT, other genes, including *Cidea*, *Dio2*, *Elovl3*, *Ppargc1a*, and *Prdm16*, were comparable between WT and PGAM5-KO adipocytes (Fig. 1*F*). Last, we performed siRNA-based transient knockdown of PGAM5 in WT adipocyte precursors to exclude the possibility of knockout line-specific effects; transient knockdown of PGAM5 also

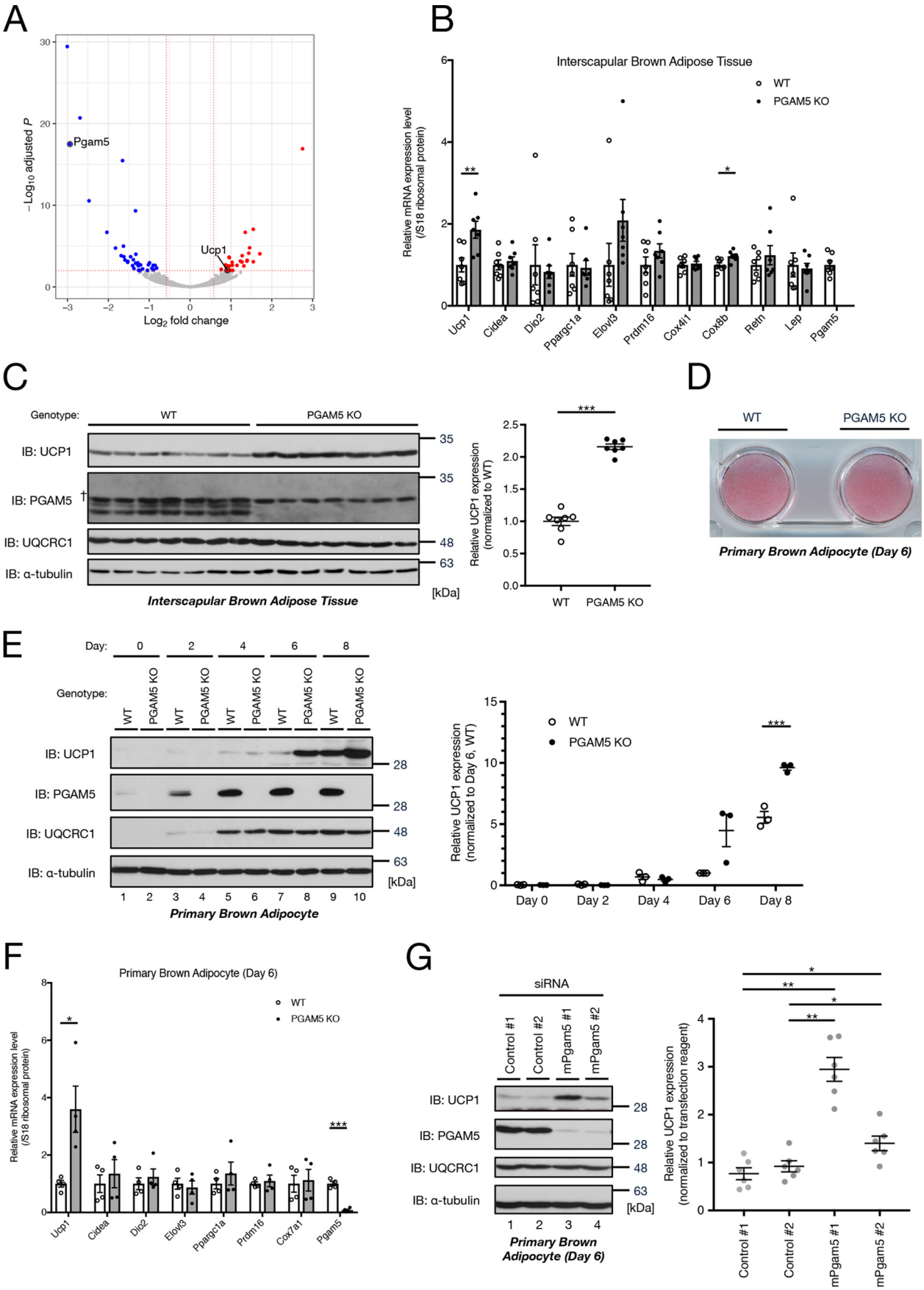
A
Pgam5
Ucp1
−Log10 adjusted P
Log2 fold change
B
Interscapular Brown Adipose Tissue
WT
PGAM5 KO
Relative mRNA expression level (/S18 ribosomal protein)
Ucp1
Cidea
Dio2
Ppargc1a
Elovl3
Prdm16
Cox4i1
Cox8b
Retn
Lep
Pgam5
C
Genotype:
WT
PGAM5 KO
IB: UCP1
IB: PGAM5
IB: UQCRC1
IB: α-tubulin
[kDa]
Interscapular Brown Adipose Tissue
Relative UCP1 expression (normalized to WT)
D
WT
PGAM5 KO
Primary Brown Adipocyte (Day 6)
E
Day:
Primary Brown Adipocyte
Relative UCP1 expression (normalized to Day 6, WT)
Day 0
Day 2
Day 4
Day 6
Day 8
F
Primary Brown Adipocyte (Day 6)
G
siRNA
Control #1
Control #2
mPgam5 #1
mPgam5 #2
Primary Brown Adipocyte (Day 6)
Relative UCP1 expression (normalized to transfection reagent)

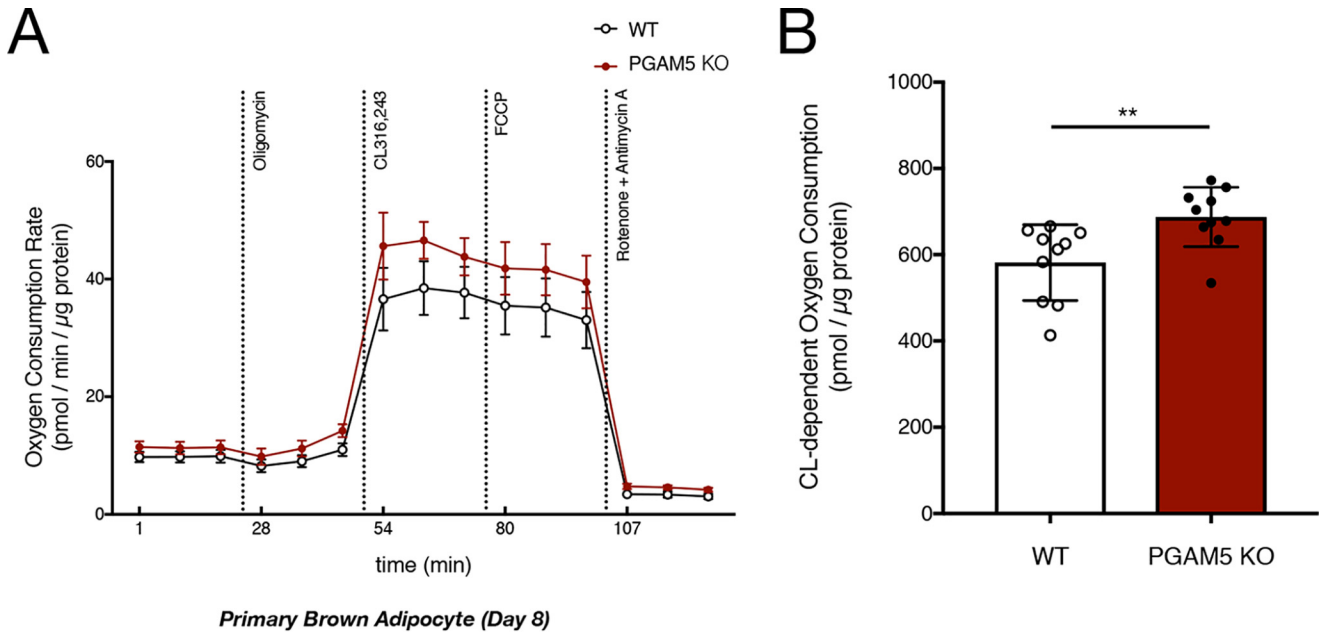

Figure 2. PGAM5 deficiency enhances oxygen consumption in brown adipocytes. *A*, oxygen consumption of WT and PGAM5-KO brown adipocytes was evaluated during the sequential addition of oligomycin, CL316,243, FCCP, and rotenone/antimycin A. *B*, CL316,243-dependent oxygen consumption was calculated as an integrated value (technical replicates: $n = 10$). Similar results were obtained in at least two additional independent experiments. Data are represented as the mean ± S.D. (*error bars*) (*A* and *B*) and individual values (*B*). **, $p < 0.01$; data were analyzed by two-tailed unpaired Student's *t* test.

resulted in increased UCP1 expression (Fig. 1*G*). These data suggest that PGAM5 depletion in brown adipocytes enhances *Ucp1* expression in a cell-autonomous manner.

PGAM5 deficiency enhances oxygen consumption in brown adipocytes

To assess the functional results of UCP1 up-regulation in PGAM5-KO brown adipocytes, we performed an oxygen consumption assay using a Seahorse XF24 extracellular flux analyzer. We evaluated the oxygen consumption rate (OCR) during the sequential addition of oligomycin, CL316,243 (a β_3-adrenergic receptor–selective agonist), carbonyl cyanide *p*-trifluoromethoxyphenylhydrazone (FCCP) and rotenone/antimycin A (Fig. 2*A*). Whereas the OCR was not largely different between WT and PGAM5-KO cells under unstimulated conditions, PGAM5-KO cells consumed more oxygen under activated conditions induced by CL316,243 (Fig. 2, *A* and *B*), suggesting that PGAM5-KO brown adipocytes have the capacity to consume more energy in response to a β_3-adrenergic receptor agonist.

PISD, a mitochondrial lipid-metabolizing enzyme, is required for PGAM5 cleavage in response to mitochondrial membrane potential loss

Next, we sought to examine the mechanism by which PGAM5 regulates UCP1 expression. It is noteworthy that PGAM5 changes its subcellular localization in accordance with its cleavage, and cleaved PGAM5 contributes to cell death and mitochondrial biogenesis (19, 25). Another group and our group previously demonstrated that PARL and OMA1 are the proteases that mediate processing of PGAM5 (23, 24); however, other regulators of PGAM5 cleavage are largely unknown. Hence, we performed a nonbiased genome-wide siRNA screen to identify new regulators of PGAM5 cleavage.

Overall, 93 and 458 genes were obtained from two statistical methods based on robust *Z* scores and *B* scores, respectively (30, 31) (Fig. 3*A*, *top* Venn diagram). Notably, both *PARL* and *OMA1* were identified using both normalization methods, confirming the reliability of the screening results (Fig. S2, *F* and *G*). Subsequently, we performed several database analyses to exclude genes whose protein products are unlikely to be localized at mitochondria. Ultimately, we identified 100 genes from the union of screened candidates identified based on robust *Z* scores and *B* scores (Fig. 3*A*, *bottom* Venn diagram). To verify the image-based screening results, we also performed immunoblotting (IB) during the secondary screening and obtained 69 candidate genes based on the combined screened candidates identified by immunocytochemistry (ICC) analysis and IB analysis (Fig. 3*B* and Table S3). It has been reported that in some cases, OXPHOS up-regulation can weaken the effects of the mitochondrial uncoupler CCCP, which results in incomplete

Figure 1. PGAM5 depletion augments UCP1 expression in brown adipocytes. *A*, a volcano plot of RNA-Seq analysis using iBAT from WT and PGAM5-KO mice. Genes with increased and decreased expression in PGAM5-KO iBAT are depicted in *red* and *blue*, respectively. *B*, qRT-PCR against the indicated genes in iBAT ($n = 7$). *Pgam5* was undetectable in PGAM5-KO iBAT. *C*, immunoblot analysis against UCP1 protein in iBAT ($n = 7$). The graph shows the quantification of the immunoblot. †, nonspecific signals. *D*, Oil Red O staining of differentiated brown adipocytes (Day 6) ($n = 3$). *E*, immunoblot analysis against the indicated proteins in brown adipocytes ($n = 3$). The same amount of protein was loaded in each *lane*. The graph shows the quantification of the immunoblot. *F*, qRT-PCR detected the indicated genes in differentiated brown adipocytes (Day 6) ($n = 4$). *G*, immunoblot analysis of the indicated genes in differentiated brown adipocytes (Day 6) ($n = 6$). The graph shows the quantification of the immunoblot. Data are represented as individual values and the mean ± S.E. (*error bars*). *, $p < 0.05$; **, $p < 0.01$; ***, $p < 0.001$; data were analyzed by two-tailed unpaired Student's *t* test (*B*, *C*, and *F*), Bonferroni's multiple-comparison test (*E*), or Tukey's multiple-comparison test (*G*). The data set used for normalization (mean = 1, S.D. = 0) was eliminated from the subsequent statistical analyses (*E*).

$\Delta\Psi_m$ loss (32). In these cases, the inhibitory effects of siRNA on CCCP-induced PGAM5 cleavage are not due to cleavage dysregulation but to incomplete $\Delta\Psi_m$ loss. Therefore, we re-evaluated the aforementioned 69 gene candidates by validating their effects on PGAM5 cleavage during CCCP regulation via treatment with three OXPHOS inhibitors (oligomycin A, F_O-F_1-ATPase inhibitor; rotenone, Complex I inhibitor; and antimycin A, Complex III inhibitor) (Fig. S2*H*). Fig. S2*H* shows the final top 10 positive siRNA results after the prioritization step, which includes experiments using two independent

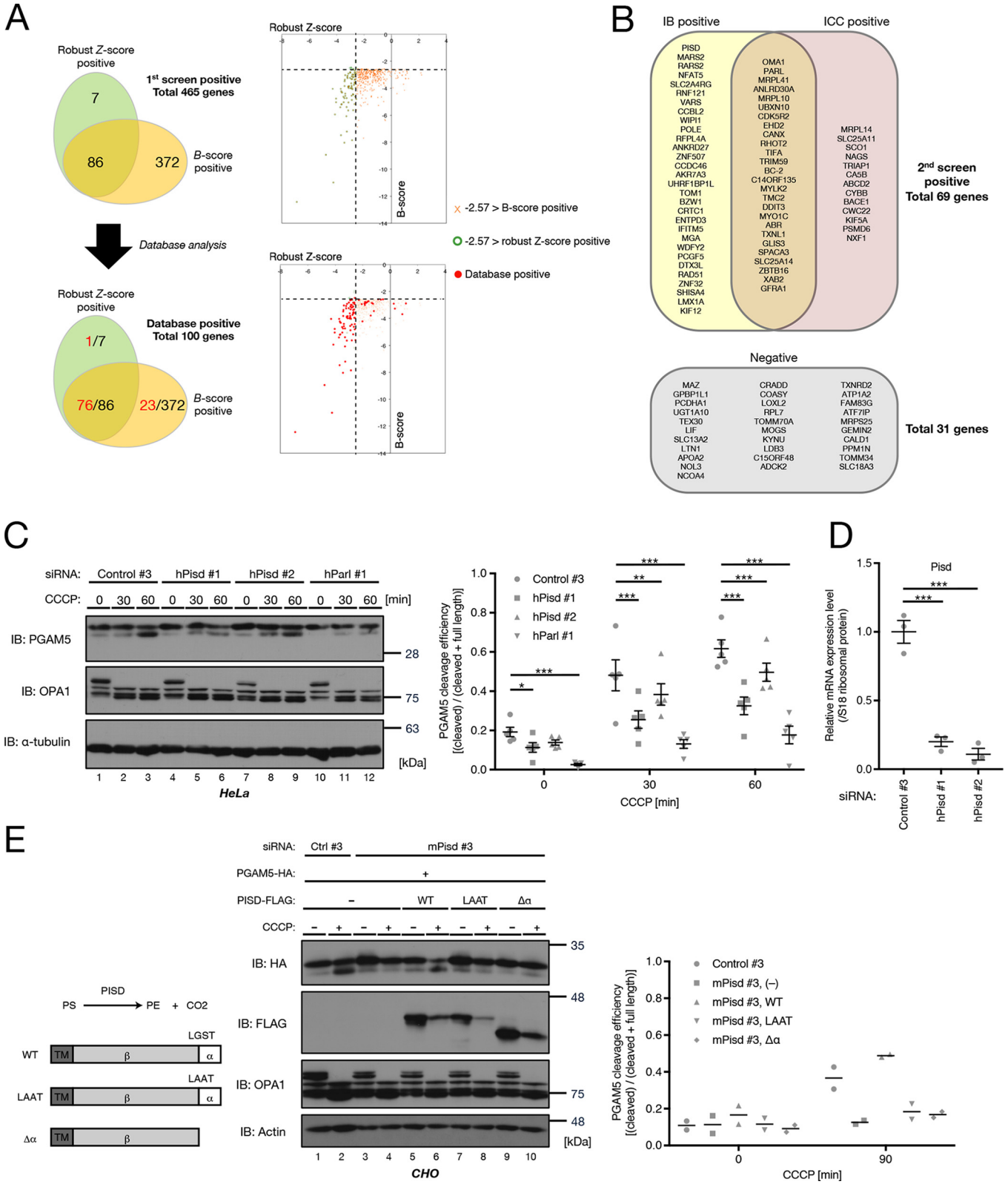

siRNAs targeting for *OMA1* and *PARL*, confirming the validity of our screening. In addition to *OMA1* and *PARL*, *PISD* was the only gene whose two independent siRNAs were ranked among the top 10 positive siRNAs (Fig. S2*H*). Therefore, we focused on PISD, as it appeared to be the strongest candidate for PGAM5 cleavage. We confirmed the aforementioned screening results using two other siRNAs targeting different regions in the *PISD* gene. Stimuli-dependent cleavage of PGAM5 was severely impaired by siRNA-mediated suppression of *PISD* expression in HeLa cells (Fig. 3*C*). Because optic atrophy protein 1 (OPA1) was also proteolytically cleaved in response to mitochondrial membrane potential loss induced by CCCP (33), OPA1 cleavage confirms successful mitochondrial membrane potential loss in the absence of PISD (Fig. 3*C*). PISD is a member of the phosphatidylserine (PS) decarboxylase family, a group of evolutionarily conserved enzymes that catalyze the formation of phosphatidylethanolamine (PE) via PS decarboxylation (34). Mammalian PISD is categorized as a Type I phosphatidylserine decarboxylases, and it localizes to the IMM (34). Although PE is also produced from ethanolamine (Etn) or Etn-phosphate via the CDP-Etn pathway, it has been reported that PISD-mediated PE synthesis is a major source of mitochondrial PE (34). Next, we examined whether PISD enzymatic activity is required for PGAM5 cleavage. Phosphatidylserine decarboxylases, including PISD, are known to be synthesized as inactive pro-enzymes, and they require posttranslational cleavage at an evolutionarily conserved LGST motif between glycine and serine, which generates α- and β-subunits and enables enzymatic activity (34, 35). The processed α subunit acts as a catalytic subunit by providing the N-terminal serine residue with a pyruvoyl group attachment site, which is required for decarboxylation. Thus, we generated two types of catalytically inactive PISD mutants, a PISD (LAAT) mutant whose LGST motif contained an LAAT sequence (36) and a PISD ($\Delta\alpha$) mutant lacking a catalytic α subunit (Fig. 3*E*). The suppression of PGAM5 cleavage in *Pisd*-knockdown CHO cells was rescued by expressing WT PISD but not by expressing catalytically inactive PISD mutants (Fig. 3*E*). These results indicate that PISD enzymatic activity is required for PGAM5 cleavage. In conclusion, we identified PISD as a regulator of PGAM5 cleavage by a genome-wide siRNA screen.

The suppressive effect on UCP1 expression requires both phosphatase activity and intramembrane cleavage of PGAM5

To confirm that the depletion of PGAM5 is the direct cause of the increased expression of UCP1, we performed adenovirus-mediated overexpression of PGAM5 in PGAM5-KO brown adipocytes. Compared with the Venus (modified GFP)-expressing cells (which were used as a negative control), PGAM5-expressing cells showed lower expression of UCP1, suggesting that PGAM5 can suppress UCP1 expression (Fig. 4*A*). Next, we asked whether the molecular functions of PGAM5 affect UCP1 expression. Previous reports revealed that PGAM5 can remove phosphates from proteins that are on serines/threonines (17) and histidines (21). It has been reported that PGAM5 facilitates mitophagy by dephosphorylating FUN14 domain–containing protein 1 (FUNDC1) (20). Another report suggested that PGAM5 dephosphorylates nucleoside diphosphate kinase B (NDPK-B) and negatively regulates $CD4^+$ T-cell functions (21). As mentioned earlier, PGAM5 is cleaved at the TM domain in response to mitochondrial stress (23, 24). A mutant that lacks phosphatase activity has already been reported (17), but a cleavage-resistant mutant has not. We have previously shown that PGAM5 is cleaved between Ser-24 and Ala-25 of the TM domain by PARL, which belongs to the rhomboid protease family (23). According to a previous study on the recognition motif of bacterial rhomboid protease (37), a small amino acid residue immediately before the cleavage site is essential for substrate recognition. This amino acid destabilizes the α-helix of substrates and is recognized by rhomboid proteases. To avoid cleavage by rhomboid proteases, we mutated Ser-24 of PGAM5 to phenylalanine, glutamate, lysine, methionine, and tryptophan based on the results of bacterial rhomboid protease (37). We found that the S24W mutant is highly resistant to cleavage induced by CCCP in HeLa cells (Fig. 4*B*). To exclude the possibility that the S24W mutant is not targeted to the mitochondria, we determined the localization by trypsin digestion of crude mitochondria suspension. The S24W mutant was digested more efficiently under hypotonic conditions than under isotonic conditions, suggesting that the PGAM5 S24W mutant is localized at the inner mitochondrial membrane (Fig. S3*A*). We then examined the effects of these cleavage-resistant and phosphatase-inactive mutants on UCP1 expression in brown adipocytes. Both phosphatase-inactive mutant (H105A) and cleavage-resistant mutant (S24W) were unable to suppress UCP1 expression in brown adipocytes, suggesting that both phosphatase activity and cleavage are required for PGAM5 to suppress UCP1 expression (Fig. 4*C*). Next, we examined the effect of PGAM5 cleavage on UCP1 expression by analyzing siRNA-mediated knockdown of PGAM5 cleavage regulators. We knocked down *Parl* and *Oma1* (proteases of PGAM5) and *Pisd* (a newly identified regulator of PGAM5 cleavage) in brown adipocytes, expecting UCP1 to be up-regulated following their reduction. However, we could not observe an increase in UCP1 by knockdown of these genes compared with negative controls (Fig. S3 (*B* and *C*); also see "Discussion"). Collectively, although knockdown of cleavage regulators did not produce the predicted results, these data (Fig. 4) suggest that PGAM5 sup-

Figure 3. PISD, a mitochondrial lipid-metabolizing enzyme, is required for PGAM5 cleavage in response to mitochondrial membrane potential loss. *A*, overview of the candidate genes identified during the primary screen. A Venn diagram and scatter plot show the distributions of the robust *Z*-scores and *B*-scores of the candidate genes. One hundred candidates with high probabilities of targeting mitochondria were selected following database analyses (MitoCarta, MitoMiner, PANTHER, and DAVID) from the combined list of robust *Z*-score–positive and *B*-score–positive genes. *B*, results of the secondary screening. The combined IB-positive and ICC-positive genes (69 candidates) were selected. *C*, immunoblot analysis of HeLa cells transfected with the indicated siRNAs. After 48 h, the cells were treated with 50 μM CCCP for the indicated times ($n = 5$). The graph shows the quantification of the immunoblot. *D*, qRT-PCR against *PISD* in HeLa cells treated with hPisd siRNAs ($n = 3$). *E*, immunoblot analysis of CHO cells transfected with the indicated siRNA and plasmids for 72 and 48 h, respectively. The cells were treated with 100 μM CCCP for the indicated times ($n = 2$). The graph shows the quantification of the immunoblot. Data are represented as individual values and the mean ± S.E. (*error bars*) (*C* and *D*) or as individual values and the mean (*E*). *, $p < 0.05$; **, $p < 0.01$; ***, $p < 0.001$; data were analyzed by Dunnett's multiple-comparison test, compared with control #3 (*C* and *D*).

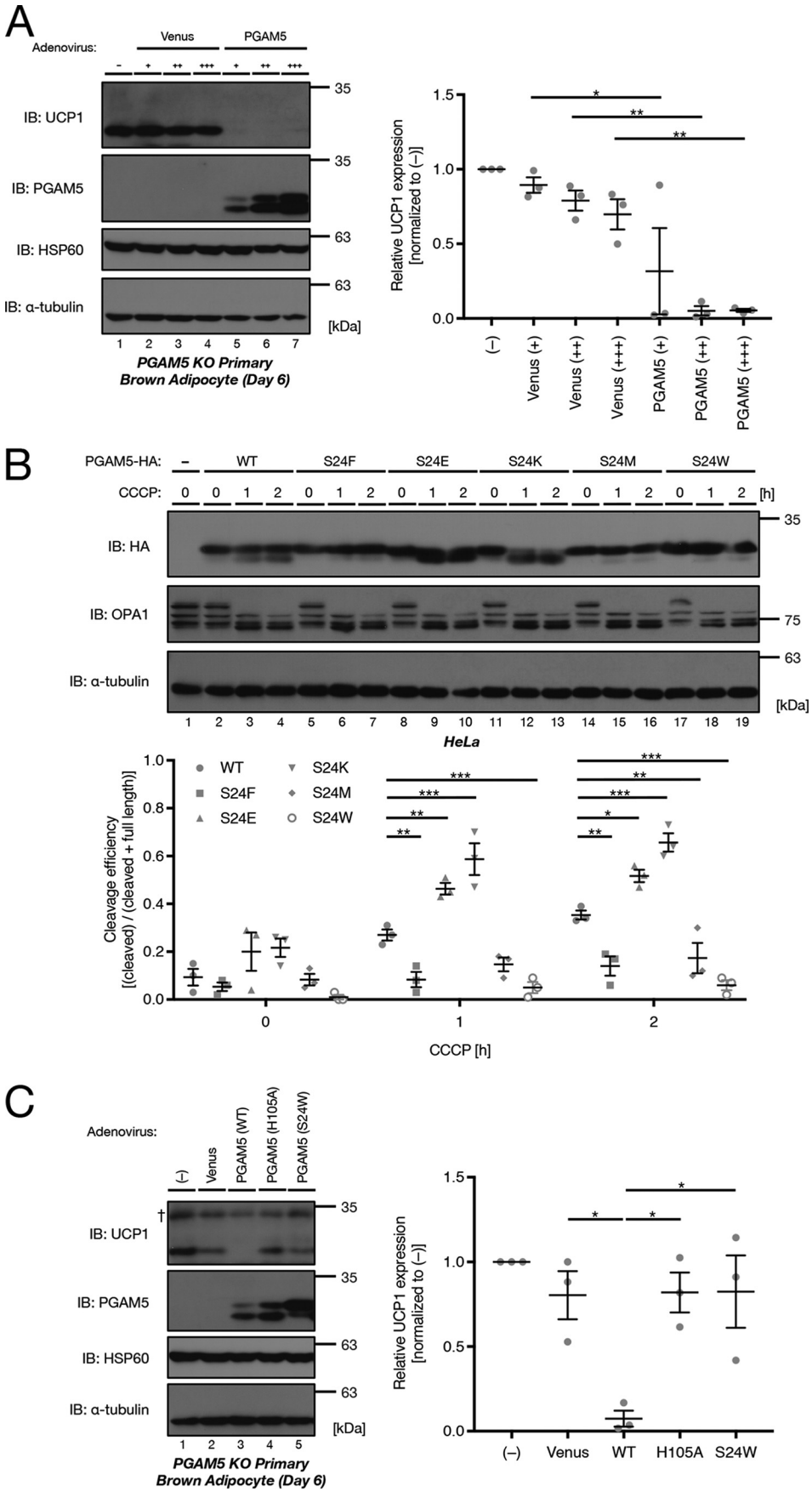
A
Adenovirus:
Venus
PGAM5
IB: UCP1
IB: PGAM5
IB: HSP60
IB: α-tubulin
[kDa]
PGAM5 KO Primary
Brown Adipocyte (Day 6)
Relative UCP1 expression
[normalized to (–)]
(–)
Venus (+)
Venus (++)
Venus (+++)
PGAM5 (+)
PGAM5 (++)
PGAM5 (+++)
B
PGAM5-HA:
WT
S24F
S24E
S24K
S24M
S24W
CCCP:
[h]
IB: HA
IB: OPA1
IB: α-tubulin
HeLa
Cleavage efficiency
[(cleaved) / (cleaved + full length)]
CCCP [h]
C
Adenovirus:
PGAM5 (WT)
PGAM5 (H105A)
PGAM5 (S24W)
IB: UCP1
IB: PGAM5
IB: HSP60
IB: α-tubulin
PGAM5 KO Primary
Brown Adipocyte (Day 6)
Relative UCP1 expression
[normalized to (–)]
H105A
S24W

presses UCP1 expression via phosphatase activity and intramembrane cleavage.

Discussion

In this study, we assessed UCP1 expression in both iBAT and iWAT from PGAM5-KO mice (Fig. 1*B* and Fig. S1*B*). There are two types of adipocytes that express UCP1 in mice: classical brown adipocytes in BAT and beige/brite adipocytes in WAT. Beige adipocytes are the inducible form of thermogenic adipocytes, which sporadically exist in WAT, possess multilocular lipid droplets, and have cristae-dense mitochondria that express UCP1 (29). According to our iWAT results, UCP1 expression is also induced in iWAT from PGAM5-KO mice (Fig. S1, *B* and *C*), suggesting that PGAM5 is a negative regulator of *Ucp1* expression even in beige adipocytes. Taken together, these results suggest that the phenotypes of PGAM5-KO mice, such as high-fat diet resistance and a decrease in lipid accumulation in iBAT (28), might be due to the increase in energy expenditure in both adipose tissues. However, it is still unclear whether up-regulated UCP1 is responsible for the phenotypes of PGAM5-KO mice. To answer this question, further investigations using adipocyte-specific PGAM5-KO mice and PGAM5 and UCP1 double-KO mice will be needed.

Consistent with the results in iBAT from mice (Fig. 1, *B* and *C*), primary cultured brown adipocytes lacking PGAM5 also showed an increase in UCP1 expression (Fig. 1, *E* and *F*). Conversely, despite the decrease in lipid accumulation in PGAM5-KO iBAT (28), lipid accumulation levels were comparable between WT and PGAM5-KO brown adipocytes. This discrepancy raises the possibility that PGAM5 deficiency in other tissues is the cause of lipid loss in iBAT, but it is potentially due to the difference in the surrounding environment of the cultured adipocytes. In iBAT, brown adipocytes are located near capillary blood vessels and are innervated by the sympathetic nervous system (38). Thus, experiments using adipocyte-specific PGAM5-KO mice will be important to answering these questions.

Because the mechanisms of PGAM5 cleavage are not fully understood, we performed a genome-wide siRNA screen to identify new regulators of PGAM5 cleavage. As a result, we identified a set of candidate PGAM5 cleavage regulators, including PISD, which is an enzyme that catalyzes the conversion of PS to PE (Fig. 3). However, the underlying mechanisms regulating PGAM5 cleavage via PISD are still unclear. We showed with a rescue experiment that the enzymatic activity of PISD is required for PGAM5 cleavage (Fig. 3*E*). Thus, it is possible that PE produced by PISD is important for the protease activity of PARL or OMA1. The rhomboid protease family, to which PARL belongs, is a member of the intramembrane cleaving protease (I-CLiP) family, which is a group of evolutionarily conserved multipass membrane proteins that catalyze the cleavage of TM domains within lipid bilayers (39, 40). As they are located within membranes, I-CLiP family members can be affected by their surrounding membrane environment. For example, after exiting the ER, the γ-secretase complex is reported to exhibit protease activity in addition to its constitutive secretory pathway role (41); the protease activity is especially present in specific membrane microdomains, such as cholesterol-rich lipid rafts (42). In a previous study, rhomboid-mediated substrate proteolysis was also found to be modulated by phospholipids, although it is unclear whether this is the case for PARL (43).

A previous report demonstrated that PISD-KO mice have an embryonic lethal phenotype (44). Mouse embryonic fibroblasts isolated from PISD-KO mouse embryos showed fragmented and dispersed mitochondria, suggesting impaired mitochondrial function (44). Recently, it was reported that heterozygous PISD mutations cause skeletal dysplasia in humans (45). Importantly, patient-derived fibroblasts showed decreased levels of OMA1 and the cleaved form of PGAM5, suggesting decreased IMM protease activity (45). These results are consistent with our finding that PISD activity is required for PGAM5 cleavage (Fig. 3), which supports the idea that PISD and its product PE are important for mitochondrial protein homeostasis in cells.

To make cleavage-resistant mutants, we mutated serine 24 in PGAM5 and found that S24F, S24M, and S24W mutants are resistant to cleavage induced by CCCP (Fig. 4*B*, *lanes 7*, *16*, and *19*). Unexpectedly, S24E and S24K mutants were susceptible to cleavage (Fig. 4*B*, *lanes 10* and *13*). These results are inconsistent with the previous report demonstrating that the charged residues inhibit the cleavage in a cell-free assay using a pair of bacterial rhomboid and substrate (37). Although the detailed mechanism is unknown, charges may have an impact on the insertion into the inner mitochondrial membrane and/or the accessibility to proteases.

Using PGAM5 mutants, we showed that PGAM5 suppresses UCP1 expression via its phosphatase activity and intramembrane cleavage (Fig. 4*C*). In terms of phosphatase activity, several responsible substrates (*e.g.* transcription factors) should regulate *Ucp1* expression. Although the physiological reason is still elusive, a recent report suggested that Lipin1 is a substrate of PGAM5 (46). Another report showed that Lipin1 is required for brown adipocyte development and function (47). Thus, Lipin1 might play a key role in PGAM5-mediated suppression of UCP1. Regarding intramembrane cleavage, a recent report suggested that cleaved PGAM5 gains the potential to be released from the mitochondria (48). It has recently been reported that the cleaved form of PGAM5 dephosphorylates

Figure 4. The suppressive effect on UCP1 expression requires both the phosphatase activity and the intramembrane cleavage of PGAM5. *A*, immunoblotting of UCP1 from differentiated PGAM5-KO brown adipocytes (Day 6), in which PGAM5 was overexpressed by adenovirus infection ($n = 3$). The graph shows the quantification of the immunoblot. *B*, immunoblot analysis of HeLa cells transfected with the indicated plasmids for 48 h. The cells were treated with 50 μM CCCP for the indicated times ($n = 3$). The graph shows the quantification of the immunoblot. *C*, immunoblot analysis to detect UCP1 in differentiated PGAM5-KO brown adipocytes (Day 6), in which WT, phosphatase-inactive mutant (H105A) or cleavage-resistant mutant (S24W) were overexpressed ($n = 3$). The graph shows the quantification of the immunoblot. †, nonspecific signals. Data are represented as individual values and the mean ± S.E. (*error bars*). *, $p < 0.05$; **, $p < 0.01$; ***, $p < 0.001$; data were analyzed by Bonferroni's multiple-comparison test (*A*), Dunnett's multiple-comparison test, compared with WT (B), or Tukey's multiple-comparison test (*C*). The data set used for the normalization (mean = 1, S.D. = 0) was eliminated from the subsequent statistical analyses (*C*). Only three pairs shown in the graph were statistically analyzed in *A*.

and stabilizes β-catenin in the cytosol, leading to intrinsic activation of Wnt signaling (25). Considering the study showing that active-Wnt signaling suppresses UCP1 expression *in vitro* and *in vivo* (49), Wnt/β-catenin signaling is a potential central player in PGAM5-mediated UCP1 suppression.

Finally, we performed knockdowns of *Parl*, *Oma1*, or *Pisd* in primary brown adipocytes to verify the importance of PGAM5 cleavage on UCP1 expression. However, we could not observe any difference in UCP1 abundance (Fig. S3*B*), presumably due to experimental limitations such as knockdown efficiency; indeed, qRT-PCR results revealed low knockdown efficiencies (Fig. S3*C*). Moreover, the cleaved form of PGAM5 is still observed even after knockdown of *Parl*, *Oma1*, or *Pisd* in primary brown adipocytes (Fig. S3*B*), suggesting an insufficient suppression of cleavage. According to a previous report, *Parl* silencing aborts adipogenesis by inhibiting PPARγ expression in 3T3-L1 cells (50). If this phenomenon also occurs even in brown adipocytes, then *Parl* knockdown in brown adipocytes should also inhibit adipogenesis, which we did not observe. For these reasons, we believe that the results shown in Fig. S3*B* do not conflict with the model that PGAM5 cleavage is important for the suppression of UCP1 expression.

In iBAT from mouse and primary cultured brown adipocytes, most of the PGAM5 was in the cleaved form (Fig. 1, *C* and *E*). We also confirmed that the bands of PGAM5 in Fig. 1*E* were detected by an AVAV antibody, which specifically recognizes the cleaved form (data not shown). Because PGAM5 is cleaved following loss of mitochondrial membrane potential, mitochondrial membrane potential levels might be decreased in differentiated brown adipocytes. It has been reported that stimulation of brown adipocytes by norepinephrine and fatty acids, which activate UCP1 and accelerate proton leakage, induces mitochondrial depolarization (51), suggesting that UCP1 activity may correlate with mitochondrial depolarization. In light of abundant UCP1 expression in differentiated brown adipocytes, the mitochondrial membrane potential may be relatively low, triggered by UCP1 activity, which may result in PGAM5 cleavage and *Ucp1* suppression. Thus, PGAM5 may play a central role in negative feedback–mediated regulation of UCP1 expression. In addition, a recent study using high-resolution MS showed that brown and beige/brite adipocytes have higher amounts of PE compared with white adipocytes (52). Hence, the abundant PE may support a negative feedback mechanism by facilitating PGAM5 cleavage.

Our findings shed light on the poorly understood function of PGAM5 in energy metabolism and provide a potential therapeutic target against obesity through brown adipocyte activation. Additionally, we hope that our screening system will provide researchers with a useful strategy for future studies attempting to identify novel protease regulators.

Experimental procedures

Antibodies and reagents

A rabbit polyclonal anti-PGAM5 antibody (RTL) was generated and has been extensively validated (17, 23, 28). The antibodies against FLAG tag (1E6) and HA tag (3F10) were purchased from Wako and Roche Applied Science, respectively. An antibody against UCP1 (ab10983) was purchased from Abcam. Antibodies against α-tubulin (sc-53029), HSP60 (sc-1052), OMA1 (sc-515788), and AIF (sc-13116) were purchased from Santa Cruz Biotechnology; an anti-UQCRC I antibody (#459140) was purchased from Invitrogen; an anti-OPA1 antibody (#612606) was purchased from BD Biosciences; an anti-actin antibody (A3853) was purchased from Sigma; Alexa Fluor 594 anti-mouse IgG (A11032) and Alexa Fluor 488 anti-rabbit IgG (A11034) were purchased from Molecular Probes; and the anti-AVAV antibody was newly generated by the following method. A pool of hybridoma cells secreting antibodies that recognize cleaved PGAM5 was generated in our previous study (K15 polyclonal antibodies (23)). In this study, we generated monoclonal hybridomas. Expansion of monoclonal hybridomas and mAb purification were performed by MBL. Briefly, after a mouse was injected with monoclonal hybridomas, the fluid in its abdomen was collected and subjected to Protein G purification. The flow-through fractions were collected and used as an AVAV mAb that specifically recognizes cleaved PGAM5. Antibodies to TOM70 and TIM23 (used in Fig. S3*A*) were kind gifts from Prof. Ishihara (Kurume University).

CL316,243 (sc-203895) was purchased from Santa Cruz Biotechnology. Oil Red O (O0625), CCCP (C2759), oligomycin A (#75351), rotenone (R8875), and antimycin A (A8674) were purchased from Sigma. FCCP (#12518) was purchased from Cayman Chemical. Hoechst 33342 (#346-07951) was purchased from Dojindo.

Cell culture and transfection

Isolation, culture, and differentiation methods of primary brown adipocytes were described previously (53). HeLa cells were cultured in Dulbecco's modified Eagle's medium with low glucose (Sigma, D6046) containing 10% fetal bovine serum in a 5% CO_2 atmosphere at 37 °C. HeLa cells stably expressing PGAM5 with a C-terminal FLAG tag (PGAM5-FLAG stable HeLa cells) were generated in our previous study (23). CHO cells, a kind gift from Dr. Kono and Prof. Arai (University of Tokyo), were cultured in Ham's F-12 medium (Wako, #087-08335) containing 10% fetal bovine serum in a 5% CO_2 atmosphere at 37 °C. The transfection of expression plasmids was performed using Polyethylenimine Max (Polysciences, #24765). Adenoviruses were produced by cloning Venus, PGAM5, PGAM5 (H105A), and PGAM5 (S24W) into pAd/CMV/V5 as described by the manufacturer (Invitrogen). For RNAi, cells were transfected with siRNAs (Dharmacon or Invitrogen) using Lipofectamine RNAiMAX transfection reagent (Invitrogen, #13778500) according to the manufacturer's instructions. Details of the siRNAs used in this work can be found in Table S2*A*.

Immunoblot analysis and immunocytochemistry

Tissues or cells were lysed with IP lysis buffer (20 mM Tris-HCl, 150 mM NaCl, 10 mM EDTA, 1% sodium deoxycholate, 1% Triton X-100) with protease inhibitors (1 mM phenylmethylsulfonyl fluoride, 5 mg/ml leupeptin). Lysates were resolved by SDS-PAGE and transferred onto polyvinylidene difluoride membranes (Millipore, IVPH00010). The membranes were blocked with 5% skim milk (Yukijirushi) in TBS-T (50 mM Tris-

HCl, 150 mM NaCl, 0.05% Tween 20) and then probed with appropriate antibodies. Antibody-antigen complexes were detected using an enhanced chemiluminescence system. For immunocytochemistry, cultured cells were fixed with 2% formaldehyde in PBS and permeabilized with 0.2% Triton X-100. After 30 min of blocking with 2% BSA in PBS, the cells were stained with the appropriate antibodies. Images were captured on a Leica TCS SP5 confocal microscope.

Expression plasmids and mutagenesis

Expression plasmids for this study were constructed by standard molecular biology techniques, and all constructs were verified by sequencing. A human PGAM5 and its H105A and S24F mutant cDNAs were previously cloned and subcloned into the vector pcDNA3/GW (Invitrogen), which has a C-terminal HA tag (17, 23). Site-directed mutagenesis of human PGAM5 was performed using the following primer and its complementary sequence primer: S24E, 5′-GCCGCCGTGCTCTTCGAGGCCGTGGCGGTAGGG-3′; S24K, 5′-GCCGCCGTGCTCTTCAAGGCCGTGGCGGTAGGG-3′; S24M, 5′-GCCGCCGTGCTCTTCATGGCCGTGGCGGTAGGG-3′; S24W, 5′-GCCGCCGTGCTCTTCTGGGCCGTGGCGGTAGGG-3′. A human *PISD* cDNA was amplified by RT-PCR from total RNA isolated from HEK293A cells, and then it was subcloned into pcDNA3/GW. cDNA encoding human PISD amino acids 1–377 (PISD Δα) was generated by PCR using human *PISD* plasmid as a template. Site-directed mutagenesis of human PISD (LAAT; Gly-377 and Ser-378 were substituted with Ala) was performed using the following primer and its complementary sequence primer: 5′-TTCAACCTGGCCGCCACCATCGT-3′.

Quantitative PCR analysis

Total RNA was isolated from tissues or cells using Isogen (Wako, #319-90211), and the RNA was reverse-transcribed with ReverTra Ace qPCR RT Master Mix with gDNA Remover (Toyobo, FSQ-301). Primers were designed using the Universal Probe Library Assay Design Center (Roche Applied Science). Quantitative RT-PCR was carried out by a LightCycler 96 (Roche Applied Science) using SYBR Green PCR Master Mix. Data were normalized to Rps18 expression. Primer sequences are listed in Table S2*B*.

Assays of crude mitochondria

Cells were collected and suspended with isotonic buffer (10 mM HEPES-KOH, 0.22 M mannitol, and 0.07 M sucrose, pH 7.4). The cell suspension was homogenized with a 27-gauge needle syringe on ice. The cell homogenate was centrifuged at 500 × *g* for 10 min at 4 °C. Supernatant was further centrifuged at 8,000 × *g* for 10 min at 4 °C. This pellet containing mitochondria was regarded as "crude mitochondria." For trypsin digestion, crude mitochondria were resuspended in the following buffers with various concentrations of trypsin (Sigma, T4799) for 30 min on ice: isotonic buffer, hypotonic buffer (10 mM HEPES-KOH, pH 7.4), or Triton X-100 buffer (1% Triton X-100, 10 mM HEPES-KOH, 0.22 M mannitol, and 0.07 M sucrose, pH 7.4).

Oil Red O staining

Mature adipocytes were washed with PBS and fixed in 10% formalin for 10 min. Cells were washed with PBS and rinsed with 60% isopropyl alcohol and were then stained with freshly prepared Oil Red O solution. After rinsing with 60% isopropyl alcohol and PBS, images were collected.

Oxygen consumption assay

OCR was measured at 37 °C using a Seahorse XF24 extracellular flux analyzer (Seahorse Biosciences). One hour before the first measurement, the cell culture medium was exchanged with Dulbecco's modified Eagle's medium (Sigma, D5030) containing 1.5 mg/liter phenol red, 2 mM sodium pyruvate, 25 mM glucose, 1 mM glutamine, and 143 mM NaCl (pH 7.4). The OCR was measured under basal conditions and during the successive addition of 4 μM oligomycin, 1 μM CL316,243, 1 μM FCCP, and a mixture of 1 μM rotenone and 1 μM antimycin A. For protein assays and genotyping, another plate was prepared. The data presented are the mean values ± S.D. of 10 replicate wells of a representative experiment. Similar results were obtained more than three times.

CL-dependent oxygen consumption was determined by calculating the area under the curve in each well from measurement #6 (just before the CL treatment) to #9 (just before the FCCP treatment) and subtracting CL-independent oxygen consumption, which was determined by multiplying the OCR of measurement #6 by time (min).

Genome-wide siRNA screen

Primary screening—Prior to primary screening, siGENOME siRNA SMARTpool reagents were prepared on assay plates as described previously; the pools consisted of four unique siRNA duplexes per gene, and they targeted 18,104 human genes (Dharmacon; Human Genome (G-005005-02), Human Drug Targets (G-004655-02), and Human Druggable Subsets (G-004675-02)) (54). Negative-control siRNA (Dharmacon siGENOME Non-Targeting siRNA Pool #1, catalog #D-001206-13) was added to 38 wells in columns 1, 2, 23, and 24 of each plate (4 μl, 1.5 pmol/well). Positive-control siRNA (Dharmacon siGENOME Human PARL siRNA SMARTpool, catalog #M-021387-01-0005) was added to 16 wells in columns 2 and 23 of each plate (4 μl, 1.5 pmol/well) (see detailed plate layout in Table S3). The negative-control siRNA and PARL siRNA were used for plate-level quality control. Six microliters of Opti-MEM containing Lipofectamine RNAiMAX (Invitrogen) (final dilution: 1:500) was added to each well of every plate using a Multidrop Combi Reagent Dispenser (Thermo Scientific). After 20 min, HeLa cells stably expressing PGAM5-FLAG were suspended in 40 μl of medium (4.0×10^4 cells) and were dispensed into the wells using the above dispenser and subjected to reverse transfection (final siRNA concentration: 30 nM). After 48 h, ~80% of the medium in each well of every plate was aspirated using an AquaMax2000 plate washer (Molecular Devices) and replaced with 40 μl of medium containing CCCP (final concentration: 30 μM) using a Multidrop Combi Reagent Dispenser. After 3 h, ~80% of the medium from each well of every plate was aspirated, and the cells were fixed with 4% formaldehyde in PBS for 10 min. Then the plates underwent six

washes with PBS using an AquaMax2000 plate washer (~80% of the liquid was aspirated per wash, and 40 μl of PBS was added to each well). The cells were subsequently permeabilized with 0.2% Triton X-100 in PBS for 10 min and subjected to nine washes with PBS. After 30 min of blocking with 2% BSA in PBS, the cells were incubated with the following primary antibodies for 12 h at 4 °C: anti-FLAG antibody (PA1-984B) (1:600, rabbit) and AVAV antibody (1:400, mouse). After nine washes with PBS, the samples were incubated with the following secondary antibodies for 1 h at room temperature: Alexa Fluor 594 anti-mouse IgG (Molecular Probes; A11032) (1:300) and Alexa Fluor 488 anti-rabbit IgG (Molecular Probes; A11034) (1:500). After nine washes with PBS, all plates were subjected to cell nuclei staining with Hoechst 33342 (DOJINDO; 0.5 μg/ml) in PBS for 10 min at room temperature. Image acquisition and subsequent analyses of the immunostained cells in each well of every plate were performed using a Cellomics ArrayScan VTI automated image analyzer (Thermo Scientific) (see below for details).

Image acquisition and high-content image analysis—Image acquisition and quantitative analysis were optimized using a Colocalization BioApplication equipped with a Cellomics ArrayScan VTI automated image analyzer (Thermo Scientific). The following four image sets per field were acquired with an XF93 filter set: Channel 1 (Ch. 1) with XF93-Hoechst for visualizing nuclear staining, Channel 2 (Ch. 2) with XF93-FITC for visualizing PGAM5-FLAG signal, Channel 3 (Ch. 3) with XF93-TRITC for visualizing AVAV signal, and Channel 4 (Ch. 4) with XF93-FITC for visualizing PGAM5-FLAG signal. The image sets were obtained from four fields per well with a 10× objective, which facilitates the analysis of ~1,000 cells/well. The exposure times were 50 ms for Ch. 1, 100 ms for Ch. 2, and 200 ms for both Ch. 3 and Ch. 4. The fluorescent nuclear signals in Ch. 1 were used to automatically define the focal planes and mark cells. Based on the nuclear regions of the target cells, the mitochondrial regions and the region of interest (ROI) for each cell were identified using the region containing a fluorescent signal derived from PGAM5-FLAG in Ch. 4, whose overlap with the nuclear region defined in Ch. 1 was excluded. To quantify PGAM5 cleavage efficiency, the ratio of average fluorescence intensity per pixel in the ROI of Ch. 3 (AVAV) to that in the ROI of Ch. 2 (PGAM5-FLAG) was calculated for each cell. The mean of this calculated value was subsequently defined as the overall PGAM5 cleavage efficiency in the well (Fig. S3*C*).

Statistical analysis of screening results—To control for screening assay quality between plates, the Z' factor was calculated for each plate using the following formula,

$$Z' \text{ factor} = 1 - 3(\sigma_p + \sigma_n)/|\mu_p + \mu_n| \quad \text{(Eq. 1)}$$

where σ_p and μ_p represent the mean and S.D. of the positive (p) control population on each plate, and σ_n and μ_n are the mean and S.D. of the negative (n) control population on each plate.

In general, when the Z' factor of an assay system is greater than 0.2, it is considered a suitable assay for high-throughput screening (55). Therefore, assay plates with Z' factors lower than 0.2 were discarded and resampled. For comparisons of sample data across assay plates, wells containing sample siRNAs, not wells containing control siRNAs, were considered to be *de facto* negative references because almost all of their genes could be irrelevant to specific biological events, such as PGAM5 cleavage (30). In this sample-based normalization, robust Z scores were calculated for each well using the following formula,

$$(X_i - \text{median}_{\text{sample}})/(\text{MAD}_{\text{sample}} \times 1.4826) \quad \text{(Eq. 2)}$$

where X_i is the summary value of PGAM5 cleavage efficiency in well i, $\text{median}_{\text{sample}}$ is the median X value in all of the sample wells on the plate, and $\text{MAD}_{\text{sample}}$ is the median absolute deviation of X in all of the sample wells on the plate.

In addition to the aforementioned robust Z scores, B scores, another normalization method, were calculated to minimize positional effects within each plate (30, 31) because the cleavage efficiency in the outer rows and columns tended to be greater than it was in the interior wells, although B scores exhibited lower sensitivities than robust Z scores in some cases. Robust Z scores or B scores < -2.57 ($p < 0.01$) were considered positive hits. According to these criteria, 93 and 485 genes were considered robust Z score–positive hits and B score–positive hits, respectively. Consequently, 465 candidate genes were identified via primary screening (Fig. 3*A* and Fig. S2 (*E–G*)).

Database analysis—Because large numbers of gene candidates were identified via primary screening, we performed database analysis to identify genes whose protein products are likely to target the mitochondria. First, using the intersection of robust Z score–positive hits and B score–positive hits, we excluded 86 genes encoding proteins with low probabilities of mitochondrial localization based on the gene functional classifications (cellular components and molecular functions) annotated in the following databases: DAVID (RRID:SCR_001881) (56, 57), PANTHER (RRID:SCR_004869) (58, 59), and LOCATE (RRID:SCR_007763) (60, 61). Then 10 genes encoding secreted proteins or cell membrane proteins were excluded; thus, 76 genes were selected from the intersection of robust Z score–positive hits and B score–positive hits. Next, based on the combination of robust Z score–positive hits and B score–positive hits, but not the intersection of these hits, we identified 379 genes encoding proteins with a strong possibility of mitochondrial localization. We employed two databases, MitoMiner (RRID:SCR_001368) (62) and MitoCarta (RRID:SCR_018165) (63, 64), because these databases provide information regarding mitochondrial localization of genes of interest based on experimental data, such as comprehensive mass spectrometric analysis of isolated mitochondria or large-scale cellular image analysis. Ultimately, 24 of the 379 genes were identified as genes whose protein products had a high probability of mitochondrial localization. Overall, our database analysis identified 100 candidate genes.

Secondary screening—Two individual Silencer Select siRNAs (Ambion) for each of the above 100 genes were spotted into a Nunc 384-well Optical Bottom Plate (Thermo Scientific). Stealth siRNA negative-control Hi GC Duplex #3 (Ambion) and positive-control stealth human PARL siRNA (described under "Cell culture and transfection") were also used. ICC was performed using the procedure that is described under "Primary screening," although a different siRNA concentration was

used (final concentration: 40 nM). To verify the image-based screening results, we also performed IB analysis during the second screening. Eight microliters of Opti-MEM containing each siRNA was spotted onto a 96-well plate (BD falcon) (final concentration: 40 nM), and 12 μl of Opti-MEM containing Lipofectamine RNAiMAX (Invitrogen) (final dilution: 1:500) was added using a Multidrop Combi Reagent Dispenser. After 20 min, HeLa cells suspended in 80 μl of medium (1.5×10^4 cells) were dispensed into each well with a Multidrop Combi Reagent Dispenser for reverse transfection. After 72 h, the media from all wells in the plate were replaced with 100 μl of medium containing CCCP (final concentration: 10 μM), and the plate was incubated at 37 °C in 5% CO_2 for 1.5 h. IB analysis was performed using the same procedure as described above. Cleavage efficiency was calculated from the band intensity of cleaved PGAM5 (upper band) relative to total PGAM5 (upper and lower band). Band intensity was measured using ImageJ software (65). During the secondary screening, each experiment was repeated to determine data reproducibility (ICC was performed three times, and IB analysis was performed twice). Among the two individual siRNAs tested for each gene, final candidate genes were selected when at least one of these siRNAs was effective in all of the ICC or IB experiments (*i.e.* cleavage efficiency was lower under siRNA-treated conditions than under negative-control siRNA-treated conditions). Using the above selection criteria, 56 genes were selected as positive hits via IB, whereas 39 genes were selected as positive hits via ICC. We subsequently defined the union of these positive hits (in total, 69 genes) as the final candidate genes.

Prioritization—Prioritization of the final 69 candidate genes was performed via immunoblotting. The same procedures were used as described under "Secondary screening," although the HeLa cells were treated with 100 μM CCCP and O.R.A. (1 μM oligomycin, 5 μM rotenone, and 5 μM antimycin) for 1 h.

Animals

Ten-week-old C57BL/6J male mice that were bred in our facility were used in all experiments. The establishment of PGAM5-deficient mice has been described previously (28). Animal experiments were performed according to the procedures approved by the Graduate School of Pharmaceutical Sciences, University of Tokyo.

RNA-Seq and data analysis

Total RNA (100 ng) was used for RNA-Seq library preparation with a TruSeq Stranded mRNA Library Prep Kit for NeoPrep (Illumina, NP-202-1001). This method uses a poly(A)-oligo(dT)–based purification of mRNA, which we performed according to the manufacturer's protocol with minor modification and optimization as follows. Custom dual index adaptors were ligated to the 5′- and 3′-ends of the library, and PCR was performed for 11 cycles. Then 150-bp paired-end RNA-Seq was performed with a Hiseq 3000/4000 PE Cluster Kit (Illumina, PE-410–1001) and a Hiseq 3000/4000 SBS Kit (300 cycles) (Illumina, FC-410-1003) on a Hiseq 4000 (Illumina), according to the manufacturer's protocol. Raw paired-end 150-bp reads were aligned to the reference genome (mm10) using HISAT2 (version 2.1.0) (66). The number of reads mapped to each gene was determined by featureCounts (version 1.6.2) (67). Differential gene expression analysis was performed with the R package DESeq2 (68) in R (version 3.5.2). Cluster analysis was performed using the package MBCluster.Seq (version 1.0) (69). In this study, we removed one PGAM5-KO sample (ko4) from subsequent analyses because this sample was strongly suspected of muscle tissue contamination (data not shown).

Statistics

The results are represented as individual values and the mean ± S.E. unless otherwise indicated in the figure legends. Unpaired two-tailed Student's *t* test, Dunnett's multiple-comparison test, Tukey's multiple-comparison test, or Bonferroni's multiple-comparison test were used. Statistical analyses were performed using GraphPad Prism (version 7.0c).

Data and software availability

All software programs used in this study are listed in Table S2*C*. All raw sequencing reads and raw count matrices generated in this study are available online at NCBI GEO (GSE138782). All of the rest of the data are contained within the paper.

Author contributions—S. Sugawara, Y. K., S. Sekine, L. M., A. T., T. F., and K. H. data curation; S. Sugawara, Y. K., S. Sekine, A. T., T. F., and K. H. investigation; S. Sugawara and K. W. methodology; S. Sugawara, Y. K., S. Sekine, K. H., and H. I. writing-original draft; S. Sekine, K. H., and H. I. conceptualization; S. Sekine, T. Y., K. H., and H. I. supervision; K. H. and H. I. funding acquisition.

Acknowledgments—We thank Prof. Kohsuke Takeda for meaningful discussion. We also thank Prof. Naotada Ishihara for providing anti-TOM70 and anti-TIM23 antibodies. We also thank Dr. Nozomu Kono and Prof. Hiroyuki Arai for advice and for providing CHO cells. We thank all members of the Laboratory of Cell Signaling, particularly Dr. Isao Naguro, for fruitful discussion.

References

1. Carpentier, A. C., Blondin, D. P., Virtanen, K. A., Richard, D., Haman, F., and Turcotte, É. E. (2018) Brown adipose tissue energy metabolism in humans. *Front. Endocrinol.* (*Lausanne*) **9,** 447 CrossRef Medline
2. Bessesen, D. H., and Van Gaal, L. F. (2018) Progress and challenges in anti-obesity pharmacotherapy. *Lancet Diabetes Endocrinol.* **6,** 237–248 CrossRef Medline
3. Lowell, B. B., and Spiegelman, B. M. (2000) Towards a molecular understanding of adaptive thermogenesis. *Nature* **404,** 652–660 CrossRef Medline
4. Sidossis, L., and Kajimura, S. (2015) Brown and beige fat in humans: thermogenic adipocytes that control energy and glucose homeostasis. *J. Clin. Invest.* **125,** 478–486 CrossRef Medline
5. Cannon, B, and Nedergaard, J. (2004) Brown adipose tissue: function and physiological significance. *Physiol. Rev.* **84,** 277–359 CrossRef Medline
6. Villarroya, F., Peyrou, M., and Giralt, M. (2017) Transcriptional regulation of the uncoupling protein-1 gene. *Biochimie* **134,** 86–92 CrossRef Medline
7. Leonardsson, G., Steel, J. H., Christian, M., Pocock, V., Milligan, S., Bell, J., So, P.-W., Medina-Gomez, G., Vidal-Puig, A., White, R., and Parker, M. G. (2004) Nuclear receptor corepressor RIP140 regulates fat accumulation. *Proc. Natl. Acad. Sci. U.S.A.* **101,** 8437–8442 CrossRef Medline
8. Kiskinis, E., Hallberg, M., Christian, M., Olofsson, M., Dilworth, S. M., White, R., and Parker, M. G. (2007) RIP140 directs histone and DNA

methylation to silence Ucp1 expression in white adipocytes. *EMBO J.* **26,** 4831–4840 CrossRef Medline

9. Wang, H., Zhang, Y., Yehuda-Shnaidman, E., Medvedev, A. V., Kumar, N., Daniel, K. W., Robidoux, J., Czech, M. P., Mangelsdorf, D. J., and Collins, S. (2008) Liver X receptor α is a transcriptional repressor of the uncoupling protein 1 gene and the brown fat phenotype. *Mol. Cell Biol.* **28,** 2187–2200 CrossRef Medline
10. Dong, M., Yang, X., Lim, S., Cao, Z., Honek, J., Lu, H., Zhang, C., Seki, T., Hosaka, K., Wahlberg, E., Yang, J., Zhang, L., Länne, T., Sun, B., Li, X., Liu, Y., Zhang, Y., and Cao, Y. (2013) Cold exposure promotes atherosclerotic plaque growth and instability via UCP1-dependent lipolysis. *Cell Metab.* **18,** 118–129 CrossRef Medline
11. Feldmann, H. M., Golozoubova, V., Cannon, B., and Nedergaard, J. (2009) UCP1 ablation induces obesity and abolishes diet-induced thermogenesis in mice exempt from thermal stress by living at thermoneutrality. *Cell Metab.* **9,** 203–209 CrossRef Medline
12. Cypess, A. M., Lehman, S., Williams, G., Tal, I., Rodman, D., Goldfine, A. B., Kuo, F. C., Palmer, E. L., Tseng, Y.-H., Doria, A., Kolodny, G. M., and Kahn, C. R. (2009) Identification and importance of brown adipose tissue in adult humans. *N. Engl. J. Med.* **360,** 1509–1517 CrossRef Medline
13. Finlin, B. S., Memetimin, H., Confides, A. L., Kasza, I., Zhu, B., Vekaria, H. J., Harfmann, B., Jones, K. A., Johnson, Z. R., Westgate, P. M., Alexander, C. M., Sullivan, P. G., Dupont-Versteegden, E. E., and Kern, P. A. (2018) Human adipose beiging in response to cold and mirabegron. *JCI Insight* **3,** 121510 CrossRef Medline
14. Porter, C., Herndon, D. N., Chondronikola, M., Chao, T., Annamalai, P., Bhattarai, N., Saraf, M. K., Capek, K. D., Reidy, P. T., Daquinag, A. C., Kolonin, M. G., Rasmussen, B. B., Borsheim, E., Toliver-Kinsky, T., and Sidossis, L. S. (2016) Human and mouse brown adipose tissue mitochondria have comparable UCP1 function. *Cell Metab.* **24,** 246–255 CrossRef Medline
15. Saito, M., Okamatsu-Ogura, Y., Matsushita, M., Watanabe, K., Yoneshiro, T., Nio-Kobayashi, J., Iwanaga, T., Miyagawa, M., Kameya, T., Nakada, K., Kawai, Y., and Tsujisaki, M. (2009) High incidence of metabolically active brown adipose tissue in healthy adult humans. *Diabetes* **58,** 1526–1531 CrossRef Medline
16. Lo, S.-C., and Hannink, M. (2008) PGAM5 tethers a ternary complex containing Keap1 and Nrf2 to mitochondria. *Exp. Cell Res.* **314,** 1789–1803 CrossRef Medline
17. Takeda, K., Komuro, Y., Hayakawa, T., Oguchi, H., Ishida, Y., Murakami, S., Noguchi, T., Kinoshita, H., Sekine, Y., Iemura, S., Natsume, T., and Ichijo, H. (2009) Mitochondrial phosphoglycerate mutase 5 uses alternate catalytic activity as a protein serine/threonine phosphatase to activate ASK1. *Proc. Natl. Acad. Sci. U.S.A.* **106,** 12301–12305 CrossRef Medline
18. Wang, Z., Jiang, H., Chen, S., Du, F., and Wang, X. (2012) The mitochondrial phosphatase PGAM5 functions at the convergence point of multiple necrotic death pathways. *Cell* **148,** 228–243 CrossRef Medline
19. Zhuang, M., Guan, S., Wang, H., Burlingame, A. L., and Wells, J. A. (2013) Substrates of IAP ubiquitin ligases identified with a designed orthogonal E3 ligase, the NEDDylator. *Mol. Cell* **49,** 273–282 CrossRef Medline
20. Chen, G., Han, Z., Feng, D., Chen, Y., Chen, L., Wu, H., Huang, L., Zhou, C., Cai, X., Fu, C., Duan, L., Wang, X., Liu, L., Liu, X., Shen, Y., Zhu, Y., and Chen, Q. (2014) A Regulatory signaling loop comprising the PGAM5 phosphatase and CK2 controls receptor-mediated mitophagy. *Mol. Cell* **54,** 362–377 CrossRef Medline
21. Panda, S., Srivastava, S., Li, Z., Vaeth, M., Fuhs, S. R., Hunter, T., and Skolnik, E. Y. (2016) Identification of PGAM5 as a mammalian protein histidine phosphatase that plays a central role to negatively regulate $CD4^+$ T cells. *Mol. Cell* **63,** 457–469 CrossRef Medline
22. Holze, C., Michaudel, C., Mackowiak, C., Haas, D. A., Benda, C., Hubel, P., Pennemann, F. L., Schnepf, D., Wettmarshausen, J., Braun, M., Leung, D. W., Amarasinghe, G. K., Perocchi, F., Staeheli, P., Ryffel, B., and Pichlmair, A. (2018) Oxeiptosis, a ROS-induced caspase-independent apoptosis-like cell-death pathway. *Nat. Immunol.* **19,** 130–140 CrossRef Medline
23. Sekine, S., Kanamaru, Y., Koike, M., Nishihara, A., Okada, M., Kinoshita, H., Kamiyama, M., Maruyama, J., Uchiyama, Y., Ishihara, N., Takeda, K., and Ichijo, H. (2012) Rhomboid protease PARL mediates the mitochondrial membrane potential loss-induced cleavage of PGAM5. *J. Biol. Chem.* **287,** 34635–34645 CrossRef Medline
24. Wai, T., Saita, S., Nolte, H., Müller, S., König, T., Richter-Dennerlein, R., Sprenger, H.-G., Madrenas, J., Mühlmeister, M., Brandt, U., Krüger, M., and Langer, T. (2016) The membrane scaffold SLP2 anchors a proteolytic hub in mitochondria containing PARL and the i-AAA protease YME1L. *EMBO Rep.* **17,** 1844–1856 CrossRef Medline
25. Bernkopf, D. B., Jalal, K., Brückner, M., Knaup, K. X., Gentzel, M., Schambony, A., and Behrens, J. (2018) Pgam5 released from damaged mitochondria induces mitochondrial biogenesis via Wnt signaling. *J. Cell Biol.* **217,** 1383–1394 CrossRef Medline
26. Lu, W., Karuppagounder, S. S., Springer, D. A., Allen, M. D., Zheng, L., Chao, B., Zhang, Y., Dawson, V. L., Dawson, T. M., and Lenardo, M. (2014) Genetic deficiency of the mitochondrial protein PGAM5 causes a Parkinson's-like movement disorder. *Nat. Commun.* **5,** 4930 CrossRef Medline
27. He, G.-W., Günther, C., Kremer, A. E., Thonn, V., Amann, K., Poremba, C., Neurath, M. F., Wirtz, S., and Becker, C. (2017) PGAM5-mediated programmed necrosis of hepatocytes drives acute liver injury. *Gut* **66,** 716–723 CrossRef Medline
28. Sekine, S., Yao, A., Hattori, K., Sugawara, S., Naguro, I., Koike, M., Uchiyama, Y., Takeda, K., and Ichijo, H. (2016) The ablation of mitochondrial protein phosphatase Pgam5 confers resistance against metabolic stress. *EBioMedicine* **5,** 82–92 CrossRef Medline
29. Ikeda, K., Maretich, P., and Kajimura, S. (2018) The common and distinct features of brown and beige adipocytes. *Trends Endocrinol. Metab.* **29,** 191–200 CrossRef Medline
30. Birmingham, A., Selfors, L. M., Forster, T., Wrobel, D., Kennedy, C. J., Shanks, E., Santoyo-Lopez, J., Dunican, D. J., Long, A., Kelleher, D., Smith, Q., Beijersbergen, R. L., Ghazal, P., and Shamu, C. E. (2009) Statistical methods for analysis of high-throughput RNA interference screens. *Nat. Methods* **6,** 569–575 CrossRef Medline
31. Malo, N., Hanley, J. A., Cerquozzi, S., Pelletier, J., and Nadon, R. (2006) Statistical practice in high-throughput screening data analysis. *Nat. Biotechnol.* **24,** 167–175 CrossRef Medline
32. Lefebvre, V., Du, Q., Baird, S., Ng, A. C.-H., Nascimento, M., Campanella, M., McBride, H. M., and Screaton, R. A. (2013) Genome-wide RNAi screen identifies ATPase inhibitory factor 1 (ATPIF1) as essential for PARK2 recruitment and mitophagy. *Autophagy* **9,** 1770–1779 CrossRef Medline
33. Ishihara, N., Fujita, Y., Oka, T., and Mihara, K. (2006) Regulation of mitochondrial morphology through proteolytic cleavage of OPA1. *EMBO J.* **25,** 2966–2977 CrossRef Medline
34. Schuiki, I., and Daum, G. (2009) Phosphatidylserine decarboxylases, key enzymes of lipid metabolism. *IUBMB Life* **61,** 151–162 CrossRef Medline
35. Kuge, O., Saito, K., Kojima, M., Akamatsu, Y., and Nishijima, M. (1996) Post-translational processing of the phosphatidylserine decarboxylase gene product in Chinese hamster ovary cells. *Biochem. J.* **319,** 33–38 CrossRef Medline
36. Thanawastien, A., Montor, W. R., Labaer, J., Mekalanos, J. J., and Yoon, S. S. (2009) *Vibrio cholerae* proteome-wide screen for immunostimulatory proteins identifies phosphatidylserine decarboxylase as a novel Toll-Like receptor 4 agonist. *PLOS Pathog.* **5,** e1000556 CrossRef Medline
37. Strisovsky, K., Sharpe, H. J., and Freeman, M. (2009) Sequence-specific intramembrane proteolysis: identification of a recognition motif in rhomboid substrates. *Mol. Cell* **36,** 1048–1059 CrossRef Medline
38. Rui, L. (2017) Brown and beige adipose tissues in health and disease. *Compr. Physiol.* **7,** 1281–1306 CrossRef Medline
39. Freeman, M. (2008) Rhomboid proteases and their biological functions. *Annu. Rev. Genet.* **42,** 191–210 CrossRef Medline
40. Rawlings, N. D., and Barrett, A. J. (1994) Families of serine peptidases. *Methods Enzymol.* **244,** 19–61 CrossRef Medline
41. Morohashi, Y., and Tomita, T. (2013) Protein trafficking and maturation regulate intramembrane proteolysis. *Biochim. Biophys. Acta* **1828,** 2855–2861 CrossRef Medline
42. Vetrivel, K. S., and Thinakaran, G. (2010) Membrane rafts in Alzheimer's disease β-amyloid production. *Biochim. Biophys. Acta* **1801,** 860–867 CrossRef Medline

43. Urban, S., and Wolfe, M. S. (2005) Reconstitution of intramembrane proteolysis *in vitro* reveals that pure rhomboid is sufficient for catalysis and specificity. *Proc. Natl. Acad. Sci. U.S.A.* **102,** 1883–1888 CrossRef Medline
44. Steenbergen, R., Nanowski, T. S., Beigneux, A., Kulinski, A., Young, S. G., and Vance, J. E. (2005) Disruption of the phosphatidylserine decarboxylase gene in mice causes embryonic lethality and mitochondrial defects. *J. Biol. Chem.* **280,** 40032–40040 CrossRef Medline
45. Zhao, T., Goedhart, C. M., Sam, P. N., Sabouny, R., Lingrell, S., Cornish, A. J., Lamont, R. E., Bernier, F. P., Sinasac, D., Parboosingh, J. S., Care4Rare Canada Consortium, Vance, J. E., Claypool, S. M., Innes, A. M., and Shutt, T. E. (2019) *PISD* is a mitochondrial disease gene causing skeletal dysplasia, cataracts, and white matter changes. *Life Sci. Alliance* **2,** e201900353 CrossRef Medline
46. Okuno, H., Okuzono, H., Hayase, A., Kumagai, F., Tanii, S., Hino, N., Okada, Y., Tachibana, K., Doi, T., and Ishimoto, K. (2019) Lipin-1 is a novel substrate of protein phosphatase PGAM5. *Biochem. Biophys. Res. Commun.* **509,** 886–891 CrossRef Medline
47. Nadra, K., Médard, J.-J., Mul, J. D., Han, G.-S., Grès, S., Pende, M., Metzger, D., Chambon, P., Cuppen, E., Saulnier-Blache, J.-S., Carman, G. M., Desvergne, B., and Chrast, R. (2012) Cell autonomous Lipin 1 function is essential for development and maintenance of white and brown adipose tissue. *Mol. Cell Biol.* **32,** 4794–4810 CrossRef Medline
48. Yamaguchi, A., Ishikawa, H., Furuoka, M., Yokozeki, M., Matsuda, N., Tanimura, S., and Takeda, K. (2019) Cleaved PGAM5 is released from mitochondria depending on proteasome-mediated rupture of the outer mitochondrial membrane during mitophagy. *J. Biochem.* **165,** 19–25 CrossRef Medline
49. Kang, S., Bajnok, L., Longo, K. A., Petersen, R. K., Hansen, J. B., Kristiansen, K., and MacDougald, O. A. (2005) Effects of Wnt signaling on brown adipocyte differentiation and metabolism mediated by PGC-1α. *Mol. Cell Biol.* **25,** 1272–1282 CrossRef Medline
50. Shiau, M.-Y., Lee, P.-S., Huang, Y.-J., Yang, C.-P., Hsiao, C.-W., Chang, K.-Y., Chen, H.-W., and Chang, Y.-H. (2017) Role of PARL-PINK1-Parkin pathway in adipocyte differentiation. *Metabolism* **72,** 1–17 CrossRef Medline
51. Wikstrom, J. D., Mahdaviani, K., Liesa, M., Sereda, S. B., Si, Y., Las, G., Twig, G., Petrovic, N., Zingaretti, C., Graham, A., Cinti, S., Corkey, B. E., Cannon, B., Nedergaard, J., and Shirihai, O. S. (2014) Hormone-induced mitochondrial fission is utilized by brown adipocytes as an amplification pathway for energy expenditure. *EMBO J.* **33,** 418–436 CrossRef Medline
52. Schweizer, S., Liebisch, G., Oeckl, J., Hoering, M., Seeliger, C., Schiebel, C., Klingenspor, M., and Ecker, J. (2019) The lipidome of primary murine white, brite, and brown adipocytes—impact of β-adrenergic stimulation. *PLOS Biol.* **17,** e3000412 CrossRef Medline
53. Hattori, K., Naguro, I., Okabe, K., Funatsu, T., Furutani, S., Takeda, K., and Ichijo, H. (2016) ASK1 signalling regulates brown and beige adipocyte function. *Nat. Commun.* **7,** 11158 CrossRef Medline
54. Watanabe, K., Umeda, T., Niwa, K., Naguro, I., and Ichijo, H. (2018) A PP6-ASK3 module coordinates the bidirectional cell volume regulation under osmotic stress. *Cell Rep.* **22,** 2809–2817 CrossRef Medline
55. Zhang, J.-H., Chung, T. D. Y., and Oldenburg, K. R. (1999) A simple statistical parameter for use in evaluation and validation of high throughput screening assays. *J. Biomol. Screen.* **4,** 67–73 CrossRef Medline
56. Huang da, W., Sherman, B. T., and Lempicki, R. A. (2009) Systematic and integrative analysis of large gene lists using DAVID bioinformatics resources. *Nat. Protoc.* **4,** 44–57 CrossRef Medline
57. Huang, D. W., Sherman, B. T., Zheng, X., Yang, J., Imamichi, T., Stephens, R., and Lempicki, R. A. (2009) Extracting biological meaning from large gene lists with DAVID. *Curr. Protoc. Bioinformatics* **27,** 13.11.1–13.11.13 CrossRef Medline
58. Mi, H., Muruganujan, A., Casagrande, J. T., and Thomas, P. D. (2013) Large-scale gene function analysis with the PANTHER classification system. *Nat. Protoc.* **8,** 1551–1566 CrossRef Medline
59. Mi, H., Poudel, S., Muruganujan, A., Casagrande, J. T., and Thomas, P. D. (2016) PANTHER version 10: expanded protein families and functions, and analysis tools. *Nucleic Acids Res.* **44,** D336–D342 CrossRef Medline
60. Fink, J. L., Aturaliya, R. N., Davis, M. J., Zhang, F., Hanson, K., Teasdale, M. S., Kai, C., Kawai, J., Carninci, P., Hayashizaki, Y., and Teasdale, R. D. (2006) LOCATE: a mouse protein subcellular localization database. *Nucleic Acids Res.* **34,** D213–D217 CrossRef Medline
61. Sprenger, J., Lynn Fink, J., Karunaratne, S., Hanson, K., Hamilton, N. A., and Teasdale, R. D. (2008) LOCATE: a mammalian protein subcellular localization database. *Nucleic Acids Res.* **36,** D230–D233 CrossRef Medline
62. Smith, A. C., and Robinson, A. J. (2016) MitoMiner v3.1, an update on the mitochondrial proteomics database. *Nucleic Acids Res.* **44,** D1258–D1261 CrossRef Medline
63. Calvo, S. E., Clauser, K. R., and Mootha, V. K. (2016) MitoCarta2.0: an updated inventory of mammalian mitochondrial proteins. *Nucleic Acids Res.* **44,** D1251–D1257 CrossRef Medline
64. Pagliarini, D. J., Calvo, S. E., Chang, B., Sheth, S. A., Vafai, S. B., Ong, S.-E., Walford, G. A., Sugiana, C., Boneh, A., Chen, W. K., Hill, D. E., Vidal, M., Evans, J. G., Thorburn, D. R., Carr, S. A., and Mootha, V. K. (2008) A mitochondrial protein compendium elucidates complex I disease biology. *Cell* **134,** 112–123 CrossRef Medline
65. Schneider, C. A., Rasband, W. S., and Eliceiri, K. W. (2012) NIH Image to ImageJ: 25 years of image analysis. *Nat. Methods* **9,** 671–675 CrossRef Medline
66. Kim, D., Langmead, B., and Salzberg, S. L. (2015) HISAT: a fast spliced aligner with low memory requirements. *Nat. Methods* **12,** 357–360 CrossRef Medline
67. Liao, Y., Smyth, G. K., and Shi, W. (2014) featureCounts: an efficient general purpose program for assigning sequence reads to genomic features. *Bioinformatics* **30,** 923–930 CrossRef Medline
68. Love, M. I., Huber, W., and Anders, S. (2014) Moderated estimation of fold change and dispersion for RNA-seq data with DESeq2. *Genome Biol.* **15,** 550 CrossRef Medline
69. Si, Y., Liu, P., Li, P., and Brutnell, T. P. (2014) Model-based clustering for RNA-seq data. *Bioinformatics* **30,** 197–205 CrossRef Medline